Flexible, Polarization-Diverse UWB Antennas for Implantable Neural Recording Systems

Hadi Bahrami, S. Abdollah Mirbozorgi, Reza Ameli, Leslie A. Rusch, and Benoit Gosselin

Flexible, Polarization-Diverse UWB Antennas for Implantable Neural Recording Systems

H. Bahrami, *Student Member, IEEE*, S.A. Mirbozorgi, *Student Member, IEEE*, R. Ameli, , *Student Member, IEEE*, L.A. Rusch, *Fellow, IEEE and* B. Gosselin, *Member, IEEE*
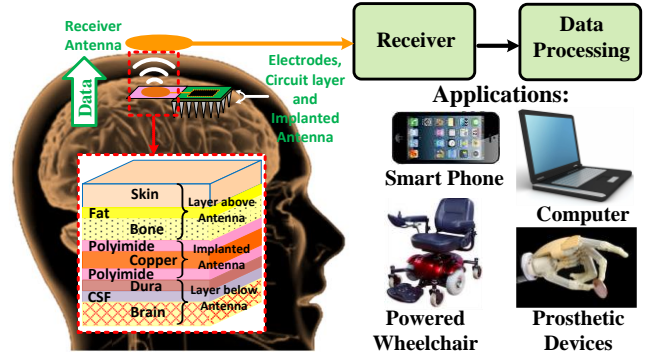

Fig. 1. Overview of implanted neural recording systems, applications and multi-layer model of the human head tissues used for designing the implanted antenna [18].

Abstract— Implanted antennas for implant-to-air data communications must be composed of material compatible with biological tissues. We design single and dual-polarization antennas for wireless ultra-wideband neural recording systems using an inhomogeneous multi-layer model of the human head. Antennas made from flexible materials are more easily adapted to implantation; we investigate both flexible and rigid materials and examine performance trade-offs. The proposed antennas are designed to operate in a frequency range of 2–11 GHz (having S_{11} below -10dB) covering both the 2.45 GHz (ISM) band and the 3.1–10.6 GHz UWB band. Measurements confirm simulation results showing flexible antennas have little performance degradation due to bending effects (in terms of impedance matching). Our miniaturized flexible antennas are 12 mm × 12 mm and 10 mm × 9 mm for single- and dual-polarizations, respectively. Finally, a comparison is made of four implantable antennas covering the 2-11 GHz range: 1) rigid, single polarization, 2) rigid, dual polarization, 3) flexible, single polarization and 4) flexible, dual polarization. In all cases a rigid antenna is used outside the body, with an appropriate polarization. Several advantages were confirmed for dual polarization antennas: 1) smaller size, 2) lower sensitivity to angular misalignments, and 3) higher fidelity.

Index Terms—Flexible antenna, Neural recording system, Implantable antenna, Dual-polarization, Single-polarization, Ultra-wideband, Near-Field, Biological tissues, Average specific absorption rate (ASAR).

I. INTRODUCTION

THERE is growing demand for implant-to-air wireless links to extract the neural activity data gathered from implanted monitoring systems [1-7]. Fig. 1 illustrates a neural recording application that requires a wireless link to transmit telemetry data between the implanted device and an external controller. In this application, an energy efficient and high-capacity link is required when several reading electrodes are interfaced to the brain. Ultra-wideband (UWB) and 2.45 GHz ISM signals are transmitted in the unlicensed Federal Communications Commission (FCC) approved frequency ranges of 3.1-10.6 GHz and 2.4-2.5 GHz respectively. UWB offers several advantages over the conventional narrowband systems such as

higher bit-rates, lower power consumption, smaller antennas, and less complexity on the transmitter side [5-7]. We design antennas supporting both 1) UWB signals for the high-bit-rate back telemetry link [7] of the neural recording sensor data and 2) 2.45GHz signals for low-bit-rate forward link [7] of control/stimulus signals.

Miniature antennas surrounded by biological tissues have a very different radiation pattern and return loss compared to those in free-space [8-11]. The characteristic impedances of biological tissues vary considerably, so careful antenna impedance matching is required. Return loss must be calculated in the presence of biological tissues around the antenna [8-11]. Additionally the brain tissues are physically sensitive in nature and flexible antennas, being more supple and more easily introduced into surrounding tissue, are highly suitable for use in implanted systems [12, 13]. Different wearable flexible antennas have been designed taking into account the effects of biological tissues [14-15]. In [12, 13], different types of flexible implanted antennas were designed for the ISM and Med-Radio bands. To our knowledge, all reported implanted microstrip UWB antennas are rigid.

In our previous work, we designed a rigid single-polarization UWB microstrip antenna for neural recording systems [16-18]. Single-polarization antennas performance degrades in the presence of angular misalignment between TX and RX antennas, which dual-polarization antennas can correct [19-22]. Most narrowband flexible implanted antennas reported in the literature are single-polarization [12-13]. Implantable antenna with flexible substrates to be placed inside the head must be biocompatible, and as thin and as soft as possible. In [23-24], a type of Kapton polyimide substrate showed these features.

In this work, we employed the same substrate as used in [23, 24]. The copper (antenna) on this substrate is covered by an identical layer of polyimide as is the superstrate. In section II, we present the simulated dielectric tissues used as the human head model. In section III we describe the antenna design methodology. Section IV presents simulation and measurement results. Performances of different antennas were measured in realistic conditions by placing the antennas in fresh brain and bone tissues of a sheep, as well as fat and skin from a chicken. Reported simulation results closely match our measurements. Section V compares the flexible and rigid, single- and dual-polarization antennas in terms of 1) average specific absorption rate (ASAR), 2) power efficiency, 3) fidelity, and 4) a figure-of-merit (FoM) defined in Section V. Finally, conclusions are drawn in section VI.

II. MODELING AND METHODOLOGY

The propagation behavior of miniature antennas surrounded by biological tissues differs greatly from those in free-space due to the electrical characteristics of biological tissues [16-17]. Antennas design must take into account the effects of multiple layers of biological tissues surrounding the wireless neural monitoring systems. The disparate conductivity and dielectric constants of each tissue leads to complex RF interactions. The thickness and electrical properties of each biological tissue layer impact the overall antenna performance of the system (propagation behavior and impedance matching) [16-18]. Each biological tissue is modeled as a dispersive dielectric medium using three electrical parameters: relative permittivity, loss tangent and mass density. The inhomogeneous environment [25] compiled from multiple layers is modeled in HFSS software using stacked homogeneous layers.

The frequency-dependent relative permittivity and loss tangent of the biological tissues are provided in [26] for the entire 2-11 GHz band. The loss tangent quantifies inherent dissipation of electromagnetic wave in a dielectric. The mass density for different tissues (tissue mass per volume unit) is reported in [27]; this parameter is needed for calculating average specific absorption rate (ASAR) within HFSS. The multi-layer model [28] used to design the antennas includes brain matter, cerebro-spinal fluid (CSF), Dura, bone (skull), fat, and skin, as shown in Fig. 1. Antenna design for implanted medical devices should favor the broadside directivity [16-18], as RF signals below the TX antenna are not useful for communications, and indeed must be attenuated as much as possible to avoid tissue damage to highly sensitive brain cells.

In order to achieve the maximum coupling between TX and RX antennas, 1) their reflection coefficients (S_{11}) must be kept below -10 dB (in order to have acceptable matching with a 50-Ω impedance), 2) the implanted TX antenna near-field radiation pattern must be directed towards its broadside, and 3) the RX antenna must be positioned at the intensity peak of the radiated EM field (outside the biological tissue). Our first step is designing a 50-Ω transmission line connected to the antenna propagator, while taking into account the effect of biological tissues. The next step is finding initial dimensions
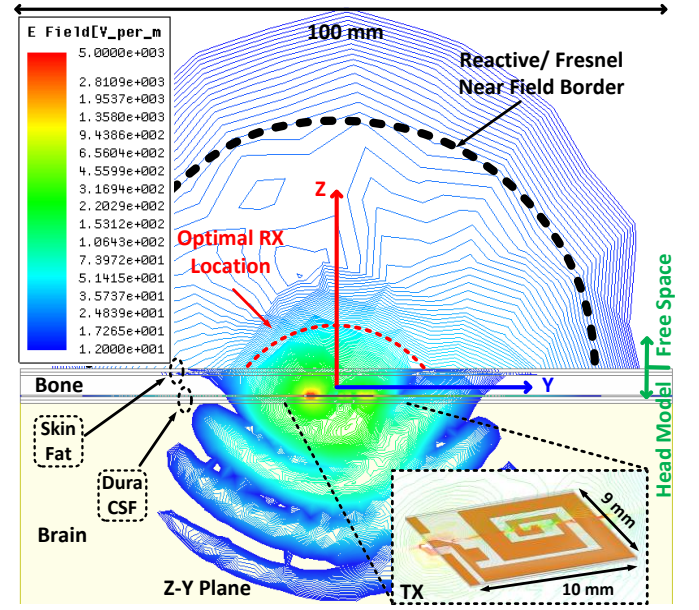

Fig. 2. Propagation behavior of E- field intensity around the implanted antenna in Z-Y plane (referenced to 1 W transmitted power by the antenna).

of the propagator to meet required specifications (i.e., S_{11} below -10 dB for both TX and RX antennas and near-field directive radiation towards the broadside of the TX antenna) at a single frequency. Next, the propagator dimensions are optimized to extend the antenna bandwidth to achieve the bandwidth of interest. Details of design are given in the next section.

HFSS provides a three-dimensional numerical solution for the electric field intensity in all tissues. A planar cross section (Z-Y plane) of the intensity is plotted in Fig. 2; the color bar shows maximum intensity in red and minimal values in blue. Each contour in the plot has E-field with a given phase, and the color along the contour changes to reflect the amplitude (referenced to a hypothetical 1 W transmitter). Note that the scale does not indicate levels for safety. Safe levels of intensity are discussed in section V. Dense contours indicate rapidly changing E-field. We used 180,000 meshes to solve our model.

Fig. 2 is illustrating the EM propagation behavior and best placement for the RX antenna. The notation along the far right of the figure indicates the border between the head tissue section and free space. This plot allows us to visualize three important aspects of the EM propagation: 1) the highest intensity of E-field and the highest RF energy absorption of head tissues (maximum ASAR), both close to the implanted antenna, 2) the transition of propagation behavior of EM waves from near-field to far-field regions for the TX antenna, and 3) the optimal location for the RX antenna outside the head.

The near field is usually subdivided into two regions: a) the reactive region, and b) the Fresnel region. In the Fresnel region, the angular distribution of the electrical intensity is directive, but varying with distance. In the reactive near-field, the electrical intensity is more spread out and nearly uniform,

with slight variations [19]. The thick dashed black curve in Fig. 2 is an approximate border between the reactive near-field and Fresnel regions based on the emerging directionality of the radiation intensity [19]. The red dashed curve in Fig. 2 indicates the region where the RX antenna will receive the strongest signal. Placing the RX antenna in this region (near-field) allows to transmit an RF signal small enough to avoid tissue damage, but strong enough for reliable wireless communications.

III. ANTENNA DESIGN

Implantable ultra-wideband antennas are subject to constraints that make their design difficult. These constraints, among others, are: 1) small footprint, 2) biocompatibility, 3) high bandwidth, and 4) flexible substrate (to avoid tissue damage). Planar monopole (single-polarization) antennas have the potential to meet these constraints for implanted biomedical systems [16-18, and 29]. However, angular misalignment between these antennas degrades the received signals heavily. In order to alleviate this problem, dual-polarization TX and RX antennas can be used [19-22]. Recently rigid single-arm spiral antennas have been used for capsule endoscopy, body area networks and implantable neural recording systems [7, 30, and 31]. The antennas presented in [30, 31] are narrowband and operate at frequencies lower than those of UWB communications. These antennas were also rigid. The rigid antenna in [7] was designed without considering the biological tissue effects. In this study we designed four types of TX antennas, two implanted single-polarization antennas (flexible and rigid) and two dual-polarization antennas (flexible and rigid). Two external single- and dual-polarization antennas were designed as RX antennas.

Our signal-polarization and dual-polarization antennas are realized as monopole microstrip and single-arm spiral antennas respectively and are covered with a biocompatible material (Kapton polyimide). For all antennas, the feed circuit is a coplanar waveguide transmission line (CPW) having 50-Ω impedance over the 2-11 GHz frequency range. We have chosen the CPW since its integration into the system, i.e., wire-bonding to the implantable chip, is convenient and straightforward. Dimensions of the CPW transmission line are designed respecting the electrical properties of its substrate as well as those of the surrounding biological tissues.

We use 0.1 mm Kapton polyimide as the biocompatible substrate for the flexible antennas. The rigid antennas have an Al_2O_3 substrate with a thickness of 0.7 mm. The relative permittivity of Kapton polyimide and Al_2O_3 is 3.5 and 9.2 respectively. For both antennas, a superstrate layer identical to their substrate layers covers the metal antenna traces. This superstrate layer completely isolated the antenna from the biological tissues making the antennas fully biocompatible.

The RX antennas, located outside the head, are less constrained in size and flexibility, so the design process is less complicated. Our RX antennas are fabricated on a FR4 substrate (relative permittivity 4.4). RX antennas have the same structure as TX antennas, however, since they do not
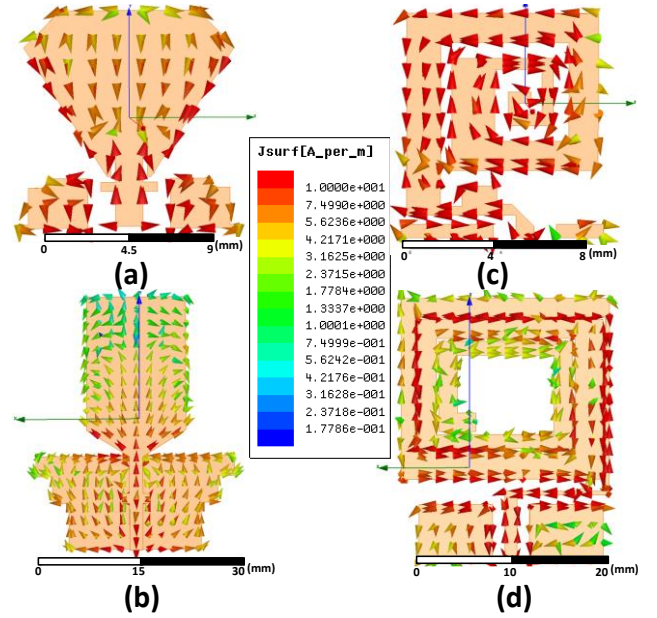

Fig. 3. The induced current on the antennas (a) TX, (b) RX for the single-polarizations, (c) TX, and (d) RX for the dual-polarizations antennas.

need to be biocompatible, they do not have the superstrate layer and they are slightly larger. A summary of our simulation in HFSS is presented in appendix II.

A. Single-Polarization Antennas

We proposed a monopole antenna that was optimized for implanted biomedical applications with a rigid substrate [16-18]. In this work, we revisited that design by incorporating a flexible substrate more suitable for neural implantation. We modified the transmission line dimensions for the TX and RX antennas to accommodate the new substrate and/or superstrate that are appropriate.

The second step of designing the antenna is designing the propagator. In single-polarization antennas, most of the induced current on the antenna surface is aligned with a single coordinate axis; this induced current is maximized in propagators with a rectangular shape planar propagator. Design starts with a rectangle, however, as the rectangular propagator is much wider than the transmission line, the return loss tends to be narrowband. We therefore taper the propagator to couple to the transmission line with the widest possible bandwidth [16-18]. Fig. 3-a and b show the induced current on the implanted (TX) antennas and external (RX) antenna. From this figure, we can see that most of the induced current on the surface of the antennas is aligned with the Y direction.

It has been shown that truncating the transmission line ground plane into a staircase shape results in better return loss [16-18]. By optimizing the width and the length of the staircase, we can reach the desired return loss in our frequency range of interest. In conclusion, to achieve: 1) S_{11} below -10 dB (for both TX and RX antennas), and 2) a near-field electrical field intensity directed towards the broadside of the TX antenna (see Fig. 2), we have optimized the physical

dimensions of the antenna.

B. Dual-Polarization Antennas

Single-polarization antennas suffer from angular misalignment [19-22], which can be overcome using dual-polarization antennas. We design two implanted dual-polarization flexible and rigid TX antennas and one rigid dual-polarization external RX antenna.

As in the previous section, the first step of design is tuning the CPW transmission line to have a 50-Ω impedance in the frequency range of interest. We incorporate a spiral propagator structure that induces a current equally on the antenna in both the horizontal and the vertical axes. The spiral structure of the propagator consists of several rectangle-shaped pieces of copper placed on the X and the Y axes with shared current.

To have equal radiated power in the X and Y directions, the total length of the rectangles in each direction must be equal. We achieve a S_{11} below -10 dB in the frequency range of interest (2-11 GHz) by matching the spiral propagator to the 50-Ω transmission line. To improve S_{11} bandwidth (while keeping it below -10 dB), the width of each rectangle in the spiral propagator is tuned. We placed the rectangular shapes as close as possible to decrease the antenna size.

During optimization of the antenna dimensions, the maximum near-field radiation intensity is checked to assure it is directed towards the broadside over the desired frequency range. Fig. 3-c and d show the induced current on implanted (TX) and external (RX) antennas. The current is distributed almost equally in the X and Y directions.

We examine the axial ratio, i.e., the ratio of orthogonal components of an E-field. To calculate the axial ratio (E_x/E_y), a single polarization antenna is needed to capture S_{21} in the X direction (representative of E_x) and S_{21} in the Y direction (representative of E_y) of the antenna of interest. For the implanted flexible TX dual polarization antenna, the external RX single polarization antenna is used. To calculate the axial ratio of the RX dual polarization antenna, the implanted flexible TX single polarization antenna is utilized.

The simulated axial ratio is shown in Fig. 4. Every attempt was made to orient antennas for maximum coupling and least insertion loss in the simulation. Because the implanted antenna is roughly three times smaller than the external antenna and the TX and RX antennas are very close to each other, Fig. 4 is our best approximation of the axial ratio.

IV. SIMULATION AND MEASUREMENT OF S-PARAMETERS

A. Measurement Setup

In order to verify our simulation results, we fabricated six antennas on different PCBs (flexible and rigid). Table I summarizes the properties of the fabricated antennas. Two of the antennas are receiver antennas (single- and dual-polarization) and the other four are the implanted transmitter antennas. A 50-Ω SMA connector connects the antenna to the measurement equipment. We used the following animal tissues: skin (0.5 mm), fat (0.5 mm), bone (3 mm), CSF (0.5 mm), Dura (0.5 mm) and brain (30 mm), thicknesses chosen to mimic typical human head tissues [28]. The S_{11} and S_{21} of the antennas are measured using a HP-8722ES network analyzer
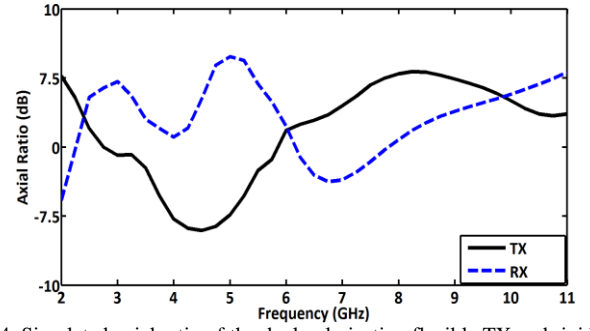

Fig. 4. Simulated axial ratio of the dual polarization flexible TX and rigid RX antennas.

TABLE I
CHARACTERISTICS OF TX AND RX ANTENNAS

Parameters						
Polarization	single	dual	single	dual	single	dual
Width (mm)	12	9	12	10	30	26.3
Length (mm)	12	10	14	11	40	30
Thickness (mm) (Substrate)	0.1	0.1	0.7	0.7	1.6	1.6
Thickness (mm) (Superstrate)	0.1	0.1	0.7	0.7	NA	NA
Permittivity	3.5	3.5	9.8	9.8	4.4	4.4
Substrate/ Location	flex/ TX	flex/ TX	rigid/ TX	rigid / TX	rigid/ RX	rigid / RX
Material	Poly-imide	Poly-imide	AL$_2$O$_3$	AL$_2$O$_3$	FR4	FR4

from 2 to 11 GHz. Fig. 5 shows the block diagram and setup used for antenna S-parameter measurements. For characterizing the flexible and rigid single-polarization TX antennas, the single-polarization RX antenna is used. For the dual-polarization TX antennas, the dual-polarization RX antenna is used. To show that the dual-polarization antennas are not sensitive to angular misalignment, we fixed the implanted TX antennas and rotated the RX antennas to three different angles (0, 45 and 90 degrees) which are illustrated in Fig. 6.

B. Flexible Single- and Dual-Polarization Antennas

Fig. 7-a shows the measured and simulated S_{11} of the single-polarization (flexible) TX and (rigid) RX antennas and Fig. 7-b shows the measured and simulated S_{11} of the dual-polarization (flexible) TX and (rigid) RX antennas. S_{11} results show good impedance matching (S_{11} below -10 dB) across the 2-11 GHz frequency range. From a practical point of view, the discrepancies between the simulation and measurement of S_{11} results are not important as long as S_{11} remains below -10 dB. Fig. 7-a and b clearly show that simulated S_{11} acceptably predicts the behavior of the antennas in measurements (below -10 dB).

Contrary to S_{11}, the frequency behavior of S_{21} is important since it is the wireless channel frequency response. Fig. 7-c and d present simulation and measurement results of S_{21} (amplitude) for the antennas. For all antennas the S_{21}
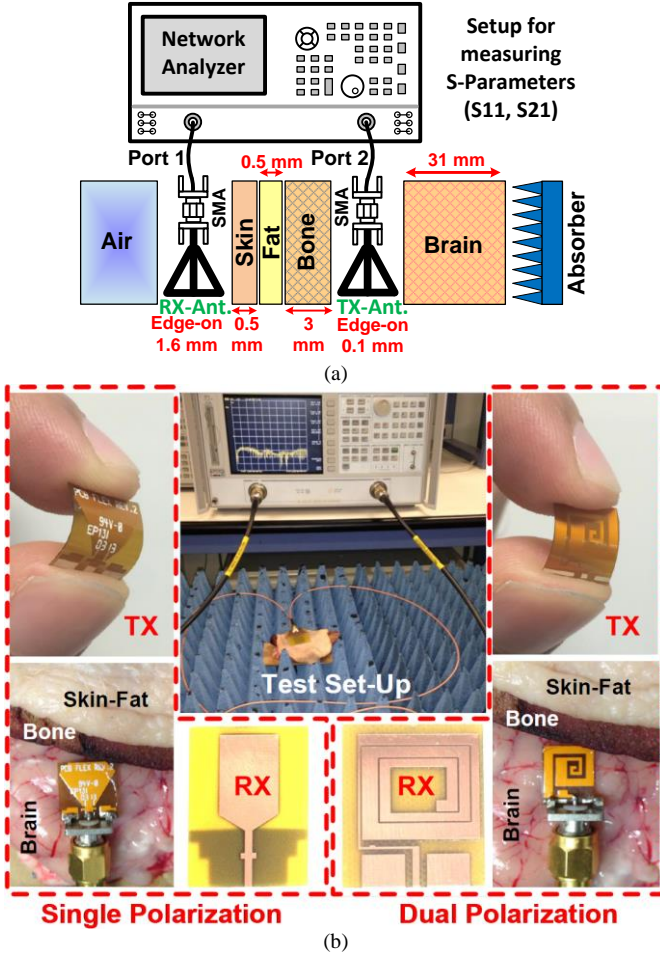
Fig. 5. S-parameter measurement (a) Block diagram of the set-up, and (b) the set-up, for S-parameter measurements.
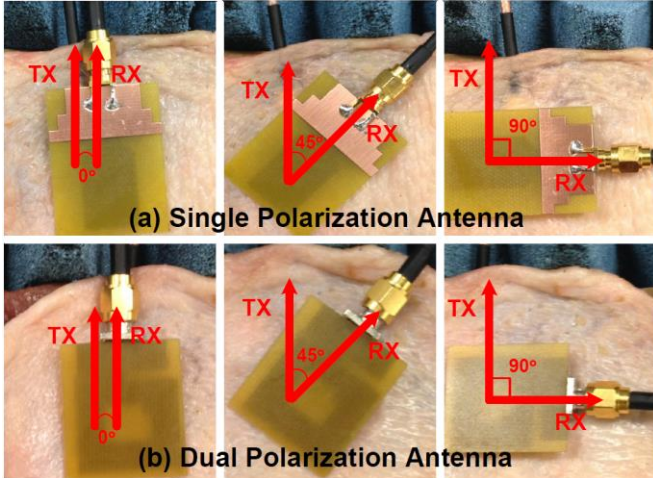

Fig. 6. Set up for characterizing sensitivity to angular misalignment between TX and RX antennas (a) single-polarization antennas, and (b) dual-polarization antennas.
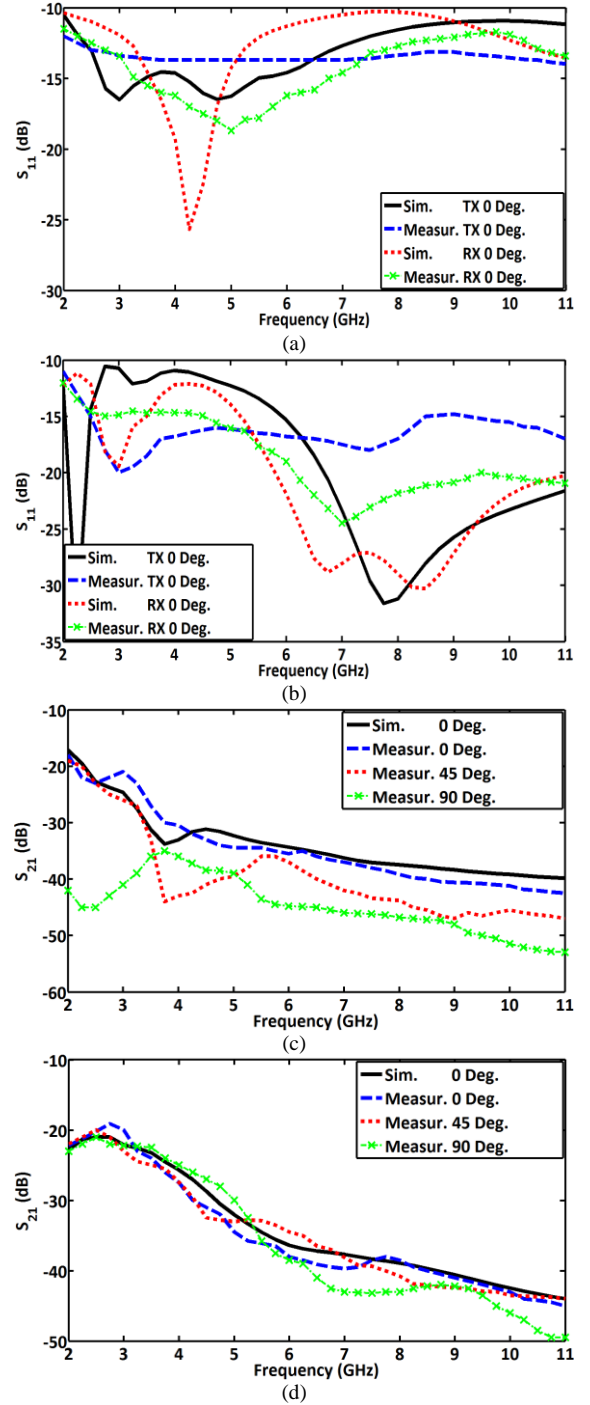

Fig. 7. Simulated and measured S-parameters for implanted flexible antennas for different miss angular alignment between TX and RX (a, c) single-polarization, and (b, d) dual-polarization.

simulation and measurement results follow the same trend.

For both polarizations, HFSS simulations and experimental results agree. Sources of small differences between the measured and the simulation results can be attributed to: 1) inevitable deviations of electrical parameters of the test setup from the simulated model because of animal age, temperature, time passed since animal death, etc. [32-33], 2) parasitic

effects caused by soldering the SMA connector to the PCB and PCB fabrication error, 3) uncertainty in reported electrical parameters in the literature [34], and 4) residual error in HFSS numerical solutions. Despite these issues and inaccuracies, the HFSS simulations predict the antenna performance well. The lower S_{21} values at lower frequencies indicate that the body has lower loss at these frequencies. This frequency band should be exploited for implant-to-air communications. As shown in Fig. 7-c and d, when the RX antenna is rotated the
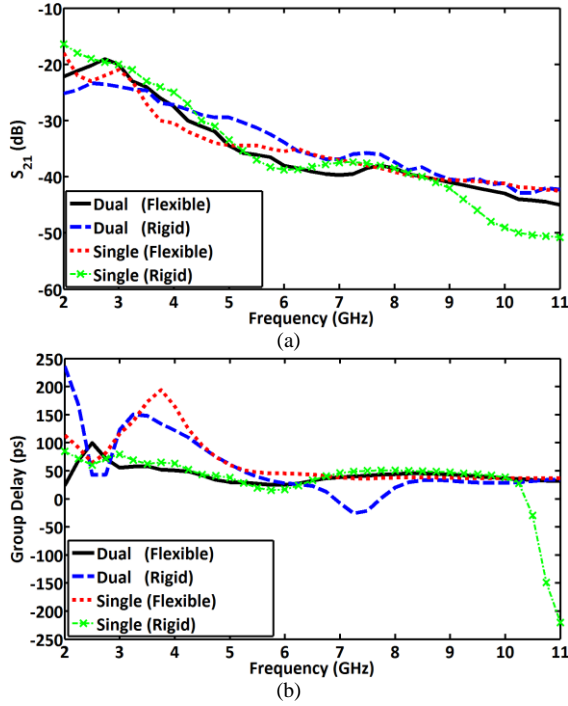
(a)

(b)

Fig. 8. Comparison of the measured results of the antennas (a) S₂₁, and (b) group delay.

dual-polarization antennas have almost the same insertion loss.

C. Comparing Flexible and Rigid Antennas

Finally, Fig. 8 presents measurements demonstrating that there is no significant compromise in performance due to the use of a flexible substrate. Antennas are designed as described in section III to the same performance targets and are implemented on both flexible and rigid substrates. In total four antennas are fabricated as both single and dual polarization are investigated. In Fig. 8-a, we see almost indistinguishable performance for all four antennas, all of which achieve our goal for S_{11} below -10 dB in the 2-11 GHz frequency range. The measured group delay in Fig. 8-b shows that the flexible dual-polarization antenna exhibits the best performance of the four antennas, introducing little pulse distortion across the entire UWB frequency band. In conclusion, flexible and rigid antennas have similar efficiency, while in our opinion, flexible antennas are likely to offer less risk of tissues damage.

V. NEAR-FIELD CHARACTERISTICS OF ANTENNAS

In near-field communications, the close proximity of the transmitter and receiver antennas leads to high mutual coupling between the antennas. Transmission loss is therefore not independent of the antenna effects [16-18]. In this section, we discuss the efficiency of antennas from a near-field link viewpoint. We find the ASAR and the received power when a specific signal is transmitted for each implanted antenna. Furthermore, we define fidelity and a figure-of-merit (FoM) for the near-field link.

A. Specific Absorption Rate (ASAR)

ASAR (Average Specific Absorption Rate) describes the
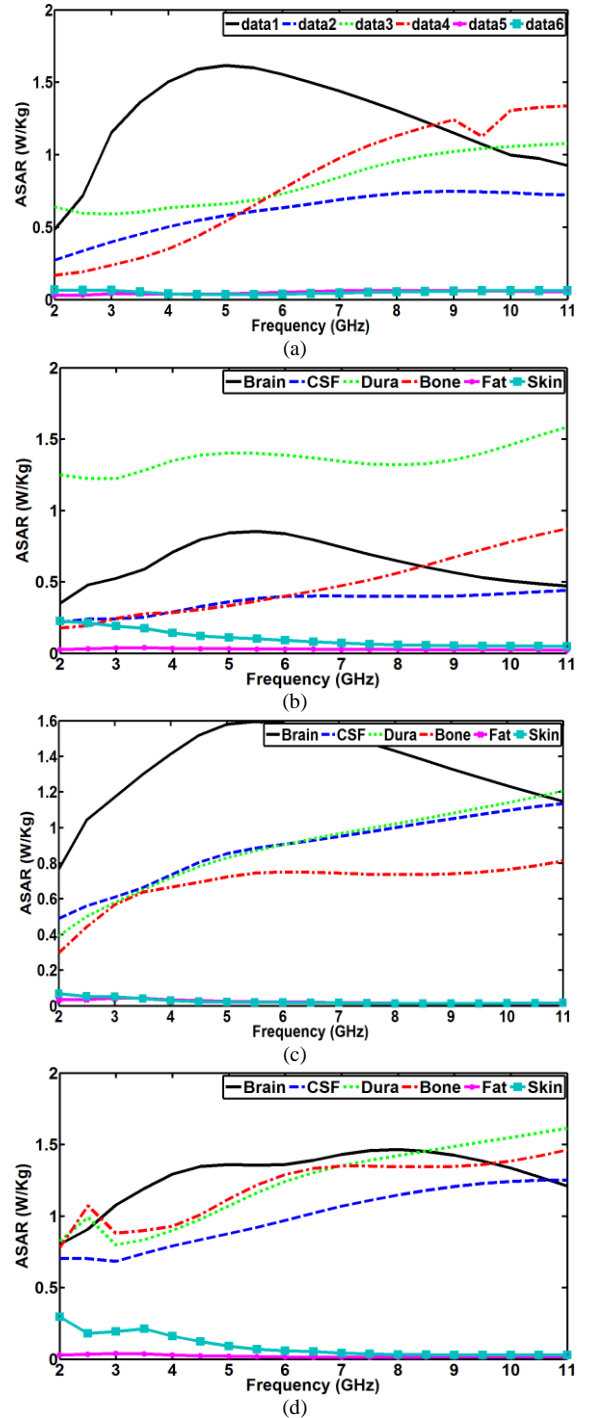

(a)

(b)

(c)

(d)

Fig. 9. The simulated ASAR of the implanted antennas and calculated allowable maximum transmitted power (P_{Max}) for (a) rigid, single-polarization (P_{Max}=5mW), (b) rigid, dual-polarization (P_{Max}=3.9mW), (c) flexible, single-polarization (P_{Max}=5mW), and (d) flexible, dual-polarization (P_{Max}=5.7mW).

electromagnetic energy that is absorbed in biological tissues and is a critical parameter for assessing the tissue-safety of implant-to-air wireless communications. The peak 1-g ASAR spatial distribution versus frequency is simulated in HFSS for all four implanted antennas. The results are presented in Table II. ANSI limitations for a maximum peak 1-g ASAR of 1.6 W/kg [35] translates into different average radiated power
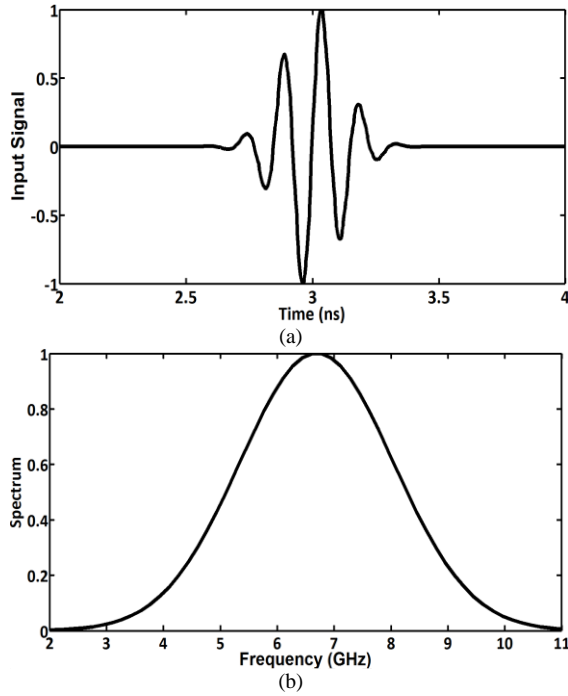
Fig. 10. (a) Waveform of the Gaussian modulated sine described by (1), and (b) its spectrum.

for each antenna: 5 mW for single-polarization flexible and rigid implanted antennas, 5.7 mW for flexible dual-polarization antennas, and 3.9 mW for rigid dual-polarization antennas. Sending more power can damage the biological tissues. Fig. 9 shows that most of the radiated power is absorbed by the brain for single-polarization and by the Dura for dual-polarization antennas.

B. Power Efficiency

Both ASAR limitations on tissue damage and FCC limitations on maximum transmitted power lead to challenging reception of UWB signals [18]. The pulse selected for transmission will influence the power efficiency. We investigate via simulation the anticipated received power when our antenna is used with a common UWB pulse shape. The excitation pulse is shown in Fig. 10-a; it consists of a Gaussian-modulated sinusoidal waveform mathematically described by [36]

$$V(t) = \sin[2\pi f_0(t - t_0)] \times e^{-\frac{(t-t_0)^2}{2\tau^2}} \qquad (1)$$

where f_0 = 6.5 GHz, τ = 120 ps and t_0 = 3 ns. This pulse has a temporal width of 0.6 ns and its frequency spectrum is centered at 6.5 GHz with a bandwidth from 2 to 11 GHz (Fig. 10-b).

MATLAB[TM] was used to characterize the performance of the near-field link using the measured S-parameters of each TX and RX antenna-pair. Simulation results include the reflected power, received power and the dissipated power. To calculate the reflected signal, the spectrum of the pulse is multiplied by S_{11}; for the received signal, the spectrum of the pulse is multiplied by S_{21}.

Table II shows the portion of the total power that is reflected from the TX antennas and received power (power efficiency)

by the RX antennas. This table also shows the amount of power dissipated in the antenna and the environment. It can be seen that the antenna reflected power is relatively low and most power is propagated. Received power is low; we note, however, that these results depend on the excitation waveforms and their spectrums, which can be optimized.

C. Fidelity Factor of the Near-field Links

System performance is optimized when the received waveform is a replicate of the transmitted waveform with no distortion. Simple design goals for amplitude and group delay attempt to minimize the distortion. Unlike narrowband antennas, UWB antennas can significantly alter transmitted pulses, due to considerably different behavior across the wide frequency band [37-38]. The antenna fidelity factor (in the far-field) captures the similarity between the *ideal expected output* waveform of an antenna and the actual radiated waveform. The antenna is assumed to introduce one of three effects (replication, integration or derivation), which we refer to as the *antenna effect*, that is incidental to the design process. For a given pulse shape, the result of an ideal antenna effect acting on that pulse shape is different from the actual radiated waveform. The fidelity factor is defined as the maximum cross-correlation between the ideal and the actual radiated waveforms when both waveforms are normalized by their energies [36-39]. Fidelity varies between zero and one, with one showing the minimum and zero showing the maximum distortion introduced by the antenna.

The impact of UWB transmit antenna geometry, material, current mode and transmitter impedance interact to a combined effect that might introduces integration or derivation instead of simple replication [37-38]. More importantly, the TX antenna can interact with other system components (exciting pulse shape, communications channel, and receive antenna geometry, material, etc.) to have an overall effect which we call the link effect. This behavior can be particularly influenced by operation in the near-field. We define a fidelity factor for near-field applications. Unlike the far-field definition of fidelity, our near-field definition considers the effect of the TX antenna, the radiation medium (the biological tissues) and the receiver antenna characteristics. Let $r(t)$ be the received pulse for an ideal link effect (which we assume takes one of three forms of replication, integration or derivation) for a given excitation pulse shape. Let $S_r(t)$ be the actual received waveform for that excitation pulse shape. The near-field fidelity is defined as the following assuming $r(t)$ and $S_r(t)$ have normalized energies

$$F = \max_{\tau} \int_{-\infty}^{+\infty} r(t) \times S_r(t + \tau) dt \qquad (2)$$

We examined the four transmit antennas we designed (dual/single polarization, rigid/flexible substrate) and determined the link effect for each for the near-field biological channel. As indicated in Table II, we found the single polarization, flexible substrate antenna and the dual polarization, rigid substrate antennas formed a system that replicated the transmitted signal without integration or derivation. The other two antennas formed a link whose
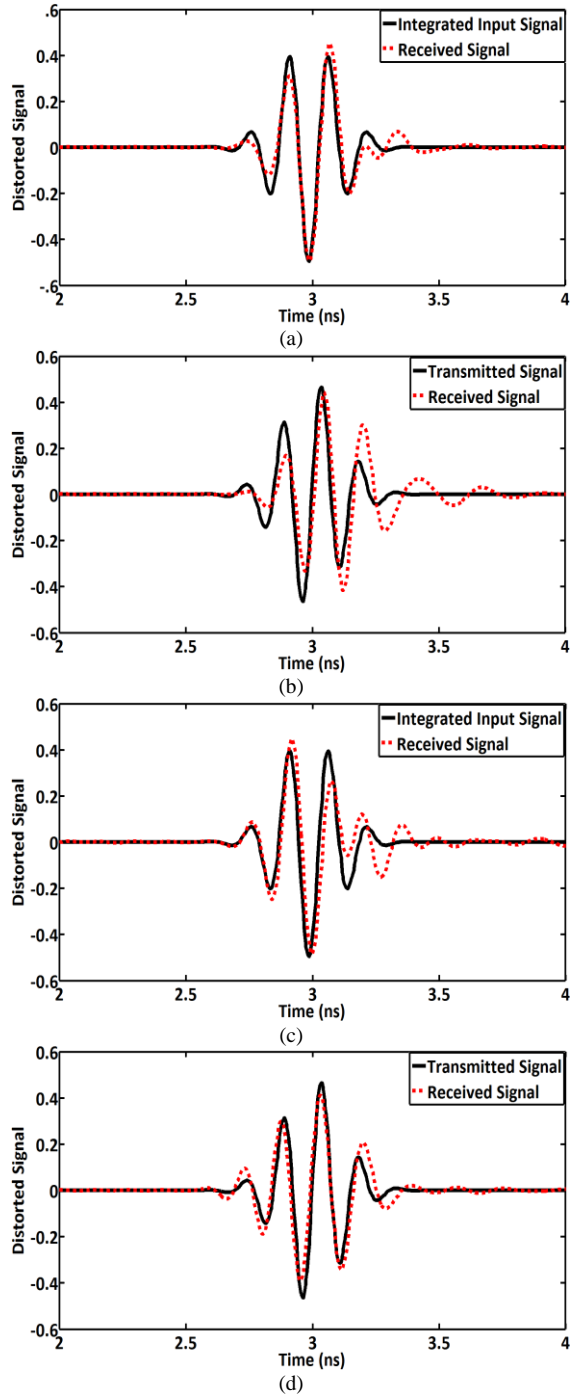
Fig. 11. Distorted received pulse which is calculated based on the measured S_{21} for antennas with (a) flexible, dual-polarization, (b) flexible, single-polarization, (c) rigid, single-polarization, and (d) rigid dual-polarization.

TABLE II
NEAR-FIELD CHARACTERISTIC OF THE ANTENNAS

Performance				
Substrate/ Polarization	flex/ single	flex/ dual	rigid/ single	rigid/ dual
Reflected Power	2.4%	2%	2.6%	2.8%
Power Efficiency	.04%	.05%	.03%	.11%
Dissipated Power	97.56%	97.95%	97.37	97.09
Link Effect	replication	integration	integration	replication
Link Fidelity	.81	.96	.84	.93
FoM	4.5	7.3	3	14.5
P_{Max} (mW)	5	5.7	5	3.9
Receiver sensitivity (dBm)	- 34.6	-31.5	-35.8	-29.7

Replication = received signal is the same as the input signal.
Integration = received signal is the integral of the input signal.

polarization antennas. In sum, the dual-polarization antennas have three advantages in comparison with the single-polarization antennas: 1) smaller size, 2) lower sensitivity to angular misalignments, and 3) higher fidelity.

D. Figure of Merit (FoM)

To compare the designed antennas in near-field applications, we propose a figure of merit (FoM). Our FoM is based on parameters that play an important role in the performance of the near-field wireless links: 1) P_e: power efficiency (%) , 2) A: TX antenna area (m^2) (RX antenna is much larger than TX antenna and changing its size does not change the link performance when it is close to a small antenna), 3) d: the distance between the RX and TX antennas which in this work is 4.0×10^{-3} m, 4) P_{Max}: maximum allowable transmitted power (mW) (according to ANSI limitations), and 5) F: fidelity factor. The FoM is defined as

$$\text{FoM} = \frac{P_e \times d \times F \times P_{Max}}{A} \qquad (3)$$

In Table II, FoM is calculated for the four designed links with different polarizations. The results show that the dual-polarization antennas have a higher FoM. As a result, this type of antenna is the best candidate for neural recording application.

E. Bending Effect

Given the size of antennas and the natural curvature of the head, at most 10 degrees of bending would be encountered in vivo. To stress our design, we examined impairments with 30 degrees of bending of the implanted antenna. The S_{11} behavior of the flexible antennas under bending is characterized and shown in Fig. 12 (the antennas are bent 30° while still

overall effect was integration. In Fig. 11 we plot $r(t)$ (solid lines) and $S_r(t)$ (dotted lines) for each of the four transmit antennas. We derive $S_r(t)$ by calculating the inverse Fourier transform of the multiplication of the pulse spectrum of (1) by the measured S_{21} of the antenna pairs. In two cases the link effect is to replicate the input transmit signal, whereas the other two integrate the input transmit signal. The fidelity factors calculated from (2) are given in Table II, showing dual-polarization antennas perform better than single-
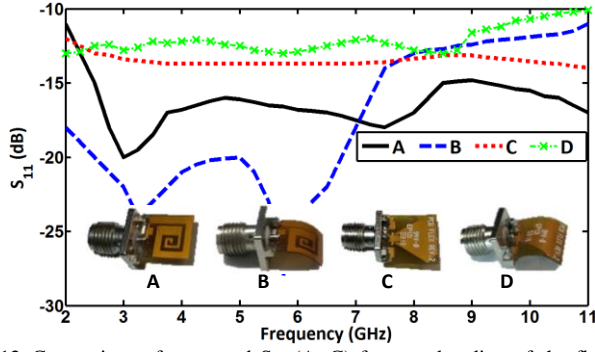
Fig.12. Comparison of measured S_{11} (A, C) for zero bending of the flexible TX antennas and (B, D) for 30 degrees bending of the flexible TX antennas.

touching the biological tissues). The results show that the S_{11} remains below -10 dB irrespective of bending. Power efficiency passed from .04% and .05% to .03% and .04% for single and dual polarization under 30 degrees flexing, respectively. Fidelity went from 0.81 to 0.72 for single polarization, and 0.96 to 0.81 for dual polarization. Finally, ASAR considerations would lead to the maximum transmit power of 5 mW reduced to 1.3 mW for single polarization, and 5.7 mW reduced to 1.5 mW for dual polarization. Bending would lead to some impairment, though parameters are still acceptable even in the extreme 30 degrees case.

VI. CONCLUSION

We presented a methodology for designing implanted single- and dual-polarization antennas on a flexible substrate for neural recording systems operating over two frequency bands (ISM and UWB). We compared single and dual polarization antennas on both rigid and flexible substrates. We found that no significant performance reduction was incurred in moving to flexible substrates that are better adapted to neurological implants. Several advantages were uncovered for dual polarization antennas: 1) smaller size, 2) lower sensitivity to angular misalignments, and 3) higher fidelity.

In near-field implant-to-air biomedical applications, the TX and RX antennas and the biological tissues between them cannot be treated separately and need to be simulated holistically. All our simulations were carried out in HFSS by exploiting an inhomogeneous, multi-layer model of biological tissues. To verify the validity of our model and the antenna design procedure, *ex vivo* measurements were made using fresh brain and bone tissues of a sheep, and fat and skin from a chicken. Measurement and simulation results are in a good agreement and validate the proposed antenna design methodology and biological tissue modeling. We investigated the maximum allowable transmitted power with respect to ANSI limitations. We also simulated and measured the biological channel overall link effect on pulse transmission and reception. Finally, in order to compare the designed antennas for near-field biological applications, a figure of merit has been suggested.

APPENDIX I

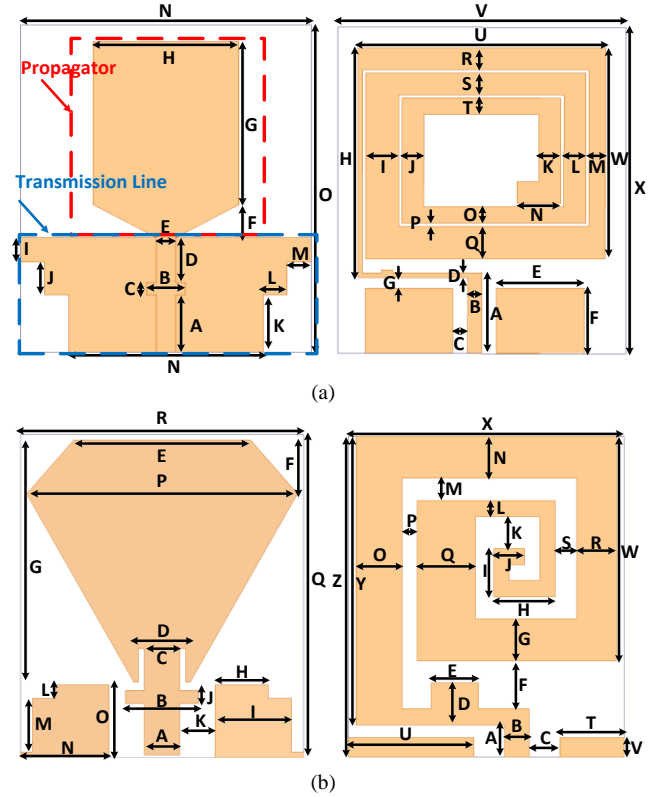The geometrical parameters of the antennas are defined in

(a)

(b)

Fig. 13. Geometric parameters (a) the RX antennas, and (b) the TX antennas.

Fig. 13 and presented in table III.

APPENDIX II

The following is a summary of our simulation in HFSS. Our excitation port was defined to include the effects of the transition from the SMA connector to the antenna. We modeled the 50-ohm SMA connector in HFSS and the port is defined as a lumped port. To model the metal, the metal thickness is set to 20 µm and the type to copper. HFSS explicitly calculates the current distribution inside the metal to yield volumetric conductor losses. Note that the "solve inside" option was alternatively employed and yielded identical results for the losses (identical S_{21}). Results were generated using discrete frequency sweeps. The frequency setting was 3 GHz for solving the mesh. Trial and error yielded six as the appropriate number of passes to achieve acceptable Max. Mag. Delta S of around .005. A second simulation was run for 6 GHz around the center frequency and identical results were obtained, validating the 3 GHz choice.

ACKNOWLEDGMENT

REFERENCES

[1] B. Gosselin, "Recent Advances in Neural Recording Microsystems," *Sensors*, vol. 11, pp. 4572,4597, 2011.

TABLE III
GEOMETRIC PARAMETERS OF THE ANTENNAS

Parameters (mm)						
Substrate/ Location	flex/ TX	flex/ TX	rigid/ TX	rigid/ TX	rigid/ RX	rigid/ RX
A	1.5	1	1.5	2	7	7.4
B	3.1	0.8	3.1	0.8	4	1.3
C	1.5	1	1.5	1	1.5	1.35
D	2.4	1.3	2.4	1.3	5.5	0.4
E	7.5	1.5	7.5	1.5	2	8
F	2	1.5	2	1.5	4	6
G	9	1.3	10	1.3	20	1
H	2.25	2	2.25	2	15	21.1
I	3.25	1.5	3.25	1.5	3	3
J	0.5	1	0.5	1	4	2
K	1.5	1	1.5	1	7	2
L	0.5	0.5	0.5	0.5	2.5	2
M	2	0.7	3	0.7	2.5	1.5
N	3.75	1.3	3.75	1.3	30	4
O	2.7	1.5	3.7	1.5	40	1.5
P	11.5	0.5	11.5	0.5	-	.3
Q	12	1.9	14	1.9	-	3
R	12	1.3	12	1.3	-	2
S	-	0.7	-	0.7	-	2
T	-	2.1	-	2.6	-	1.5
U	-	4.1	-	4.6	-	22.6
V	-	0.6	-	1.6	-	26.3
W	-	7	-	7	-	19.4
X	-	9	-	10	-	30
Y	-	9	-	9	-	-
Z	-	10	-	11	-	-

[2] B. Gosselin, A. E. Ayoub, J. F. Roy, M. Sawan, F. Lepore, A. Chaudhuri, and D. Guitton, "A Mixed-Signal Multichip Neural Recording Interface With Bandwidth Reduction, " *IEEE Transactions on Biomedical Circuits and Systems*, vol. 3, pp. 129, 141, 2009.

[3] N. M. Neihart and R. R. Harrison, "Micropower circuits for bidirectional wireless telemetry in neural recording applications," *IEEE Transactions on Biomedical Engineering*, vol. 52, pp. 1950-1959, Nov. 2005.

[4] Chow, E. Y., A. L. Chlebowski, and P. P. Irazoqui, "A miniature-implantable RF-wireless active glaucoma intraocular pressure monitor," *IEEE Transactions on Biomedical Circuits and Systems*, vol. 4, no. 6, pp. 340, 349, 2010.

[5] Gao, Y., Y. Zheng, S. Diao, W. D. Toh, C. W. Ang, M. Je, and C. H. Heng," Low-power ultrawideband wireless telemetry transceiver for medical sensor applications," *IEEE Transactions on Biomedical Engineering*, vol. 58, no. 3, 768, 772, 2010.

[6] M. S. Chae, Z. Yang, M.R. Yuce, L. Hoang, W. Liu, "A 128-Channel 6 mW Wireless Neural Recording IC With Spike Feature Extraction and UWB Transmitter," *IEEE Transactions on Neural Systems and Rehabilitation Engineering*, vol. 17, no. 4, Aug. 2009.

[7] U. M. Jow, and M. Ghovanloo, "Optimization of Data Coils in a Multiband Wireless Link for Neuroprosthetic Implantable Devices," *IEEE Transaction on Biomedcal Circuits and System*, vol. 4, no. 5, Oct. 2010.

[8] T. F. Chien, H. C. Yang, C. M. Cheng, and C. H. Luo, "Develop CPW-Fed Monopole Broadband Implantable Antennas on the High Dielectric Constant Ceramic Substrates", *Microwave and Optical Technology Letters*, vol. 52, no. 9, September 2010.

[9] M. Leib, M. Frei, D. Sailer, and W. Menzel, "Design and Characterization of a UWB Slot Antenna Optimized for Radiation in Human Tissue," *IEEE International Conference on Ultra-Wideband* (ICUWB), September 2009.

[10] T. Dissanayake, M. R. Yuce, H. Chee, "Design and Evaluation of a Compact Antenna for Implant-to-Air UWB Communication," *IEEE Antennas and Wireless Propagation Letters*, vol.8, pp.153-156, 2009.

[11] K. Y. Yazdandoost, "A 2.4 GHz Antenna for Medical Implanted Communications," *Asia Pacific Microwave Conference* (APMC), 2009.

[12] Scarpello, M.L.; Kurup, D.; Rogier, H.; Vande Ginste, D.; Axisa, F.; Vanfleteren, J.; Joseph, W.; Martens, L.; Vermeeren, G., "Design of an Implantable Slot Dipole Conformal Flexible Antenna for Biomedical Applications," *IEEE Transactions on Antennas and Propagation*, vol.59, no.10, pp.3556-3564, 2011.

[13] Alrawashdeh, R.; Huang, Y.; Cao, P., "Flexible meandered loop antenna for implants in MedRadio and ISM bands," *Electronics Letters* , vol.49, no.24, pp.1515-1517, 2013.

[14] Zheyu Wang; Lanlin Zhang; Psychoudakis, D.; Volakis, J.L., "Flexible textile antennas for body-worn communication," *Antenna Technology (iWAT), 2012 IEEE International Workshop on*, pp.205,208, 5-7 March 2012

[15] Cheolbok Kim; Jong Kyu Kim; Kyoung Tae Kim; Yong-Kyu Yoon, "Micromachined wearable/foldable super wideband (SWA) monopole antenna based on a flexible liquid crystal polymer (LCP) substrate toward imaging/sensing/health monitoring systems," *2013 IEEE 63rd Electronic Components and Technology Conference (ECTC)*, pp.1926-1932, 2013.

[16] H. Bahrami, B. Gosselin, L.A. Rusch, "Design of a miniaturized UWB antenna optimized for implantable neural recording systems," *IEEE 10th International New Circuits and Systems Conference (NEWCAS),* 17-20 June 2012.

[17] H. Bahrami, B. Gosselin, L.A. Rusch, "Realistic Modeling of the Biological Channel for the Design of Implantable Wireless UWB Communication Systems," *35th Annual International Conference of the IEEE Engineering in Medicine and Biology Society (EMBC),* August 28-September 1, 2012.

[18] H. Bahrami, S.A. Mirbozorgi, L.A. Rusch, B. Gosselin, "Biological Channel Modeling and Implantable UWB Antenna Design for Neural Recording Systems," *Biomedical Engineering, IEEE Transactions on*, vol.62, no.1, pp.88,98, Jan. 2015.

[19] Constantine A. Balanis, *Antenna Theory: Analysis and Design*, 3rd Edition, John Wiley & Sons, Inc., New York, NY, 2005.

[20] Hyung Kuk Yoon; Park A, J.A.; Young-Joong Yoon; Cheon-Hee Lee, "A CPW-fed polarization diversity antenna for UWB systems," *IEEE Antennas and Propagation Society International Symposium, AP-S 2008*, pp.1,4, 2008.

[21] Yoon, H.K.; Yoon, Y.J.; Kim, H.; Lee, C.-H., "Flexible ultra-wideband polarisation diversity antenna with band-notch function," *IET Microwaves, Antennas & Propagation,* vol.5, no.12, pp.1463,1470, 2011.

[22] L. Vallozzi, et. al., "Wireless communication for firefighters using dual-polarized textile antennas integrated in their garment," *IEEE Trans. Antennas Propag.*, vol. 58, no. 4, pp. 1357–1368, Apr. 2010.

[23] Khaleel, H.R.; Al-Rizzo, H.M.; Rucker, D.G., "Compact Polyimide-Based Antennas for Flexible Displays," *Display Technology, Journal of* , vol.8, no.2, pp.91,97, Feb. 2012.

[24] Khaleel, H.R.; Al-Rizzo, H.M.; Rucker, D.G.; Mohan, S., "A Compact Polyimide-Based UWB Antenna for Flexible Electronics," *IEEE Antennas and Wireless Propagation Letters*, vol.11, pp.564,567, 2012.

[25] C. A. Balanis, *Advanced Engineering Electromagnetics*, Wiley, 1989.

[26] S. Gabriel, R. W. Lau, and C. Gabriel, "The Dielectric Properties of Biological Tissues: III. Parametric Models for the Dielectric Spectrum of Tissues," *Physics in Medicine and Biology*, vol. 41, no. 11, pp. 2271,2293, Nov. 1996.

[27] K. Jaehoon, Y. Rahmat-Samii," Implanted antennas inside a human body: simulations, designs, and characterizations," *IEEE Transaction Microwave Theory Techniques*, vol. 52, no. 8, pp. 1934-43, 2004.

[28] A. Drossos, V. Santomaa, and N. Kuster, "The Dependence of Electromagnetic Energy Absorption Upon Human Head Tissue Composition in the Frequency Range of 300–3000 MHz," *Microwave Theory and Techniques, IEEE Transactions on*, vol.48, no.11, pp.1988,1995, Nov 2000.

[29] M. Ojaroudi, C. Ghobadi, J. Nourinia, "Small Square Monopole Antenna With Inverted T-Shaped Notch in the Ground Plane for UWB Application," *Antennas and Wireless Propagation Letters, IEEE* , vol.8, pp.728,731, 2009.

[30] W. E. Hajj, C. Person, J. Wiart , "A miniaturized rectangular-spiral Bi-band coplanar antenna for off-body communications," *2013 7th European Conference on Antennas and Propagation (EuCAP)*, pp.3262,3265, 2013.

[31] L. Sang-Heun, et. al., "A Wideband Spiral Antenna for Ingestible Capsule Endoscope Systems: Experimental Results in a Human Phantom and a Pig," *Biomedical Engineering, IEEE Transactions on* , vol.58, no.6, pp.1734,1741, June 2011.

[32] A Peyman, C Gabriel, E H Grant, G Vermeeren and L Martens "Variation of the dielectric properties of tissues with age: the effect on the values of SAR in children when exposed to walkie-talkie devices," *Physics in Medicine and. Biology*, vol. 54, pp. 227,241, 2009.

[33] A Peyman, A A Rezazadeh and C Gabriel, "Changes in the dielectric properties of rat tissue as a function of age at microwave frequencies," Physics in Medicine and. Biology, vol. 46, pp. 1617,1629, 2001.

[34] C. Gabriel and A. Peyman "Dielectric measurement: Error analysis and assessment of uncertainty", Phys. Med. Biol., vol. 51, pp.6033 ,6046 2006.

[35] "IEEE Standard for Safety Levels with Respect to Human Exposure to Radio Frequency Electromagnetic Fields, 3 kHz to 300 GHz," *IEEE Standard*, C95.1-2005, 2006.

[36] H. Kanj and M. Popovic,"A novel ultra-compact broadband antenna for microwave breast tumor detection," *PIER*, vol. 86, pp.169 -198, 2008.

[37] K. Rambabu, et. al. , "Estimation of Antenna Effect on Ultra-Wideband Pulse Shape in Transmission and Reception," *IEEE Transactions on Electromagnetic Compatibility,* vol.51, no.3, pp.604,610, Aug. 2009.

[38] A.H. Mohammadian, A. Rajkotia, and S. S. Soliman, "Characterization of UWB transmit-receive antenna system," *Ultra Wideband Systems and Technologies, 2003 IEEE Conference on*, pp.157,161, 16-19 Nov. 2003.

[39] E. Pancera and W. Wiesbeck, "Fidelity Based Optimization of UWB Antenna-Radiation for Medical Applications," *Antennas and Propagation (APSURSI), 2011 IEEE International Symposium on* , pp.2411,2414, 3-8 July 2011.

Leslie A. Rusch (S'91-M'94-SM'00-F'10) received the B.S.E.E. degree (with honors) from the California Institute of Technology, Pasadena, in 1980 and the M.A. and Ph.D. degrees in electrical engineering from Princeton University, Princeton, NJ, in 1992 and 1994, respectively. Dr. Rusch has experience in defense, industrial and academic communications research. She was a communications project engineer for the Department of Defense from 1980-1990. While on leave from Université Laval, she spent two years (2001-2002) at Intel Corporation creating and managing a group researching new wireless technologies. She is currently a Professor in the Department of Electrical and Computer Engineering at Université Laval, QC, Canada, performing research on wireless and optical communications. Prof. Rusch's research interests include digital signal processing for coherent detection in optical communications, spatial multiplexing using orbital angular momentum modes in fiber, radio over fiber and OFDM for passive optical networks; and in wireless communications, optimization of the optical/wireless interface in emerging cloud based computing networks, optical pulse shaping for high-bit rate ultrawide-band (UWB) systems, and implantable medical sensors with high bit rate UWB telemetry. She is recipient of the IEEE Canada J. M. Ham Award for Graduate Supervision. Prof. Rusch has published over 100 journal articles in international journals (90% IEEE/IEE) with wide readership, and contributed to over 130 conferences. Her articles have been cited over 3600 times per Google Scholar.

Benoit Gosselin obtained Ph.D. degree in Electrical Eng. from École Polytechnique Montréal, Canada, in 2009. He was an NSERC Post-Doctoral Fellow at the Georgia Institute of Technology in 2010. He is currently heading the Biomedical Microsystems Lab at the Depart. of ECE of Université Laval, Canada where he is an Assistant Professor. His research has generated more than 50 journal and conference articles, 4 book chapters and 3 patents. He has created several innovative wireless microelectronic systems dedicated to various implantable and wearable biomedical applications. He organized and chaired sessions in several international conferences, and he served on organization committees as well. Dr Gosselin is Chapter Chair of the IEEE Computer Society, Quebec Section and he is member of the IEEE EMBS and the IEEE CASS.

Hadi Bahrami received the B.S. and M.S. degrees in electrical engineering 2005 and 2007 from Isfahan University of Technology, Isfahan, Iran and Tarbiat Modares University, Tehran, Iran respectively. He is currently pursuing the Ph.D. degree at Biomedical Microsystems Lab, Depart. of ECE, Université Laval, Canada. His interests are RF, wireless communication systems, and integrated electro-optic circuits.

Abdollah Mirbozorgi received the B.S. degree in electrical engineering from Noshirvani University of Technology, Iran, in 2008, the M.S. degree in electrical engineering from Ferdowsi University of Mashhad, Iran, 2011, and is currently pursuing the Ph.D. degree at Biomedical Microsystems Lab, Depart. of ECE, Université Laval, Canada. His interests are neural and bionic implants, wireless implantable biomedical systems, integrated analog circuit design, and wireless power/data transmission.

Reza Ameli received the B.S. degree in electrical engineering with major in telecommunications from Ferdowsi University of Mashhad in 2012. He is currently a M.S student at Biomedical Microsystems Lab, Department of ECE, and Université Laval, Canada. His research interests include system design of neural signal acquisition chains, optogenetic stimulation neural signal processing.